AGU100 ADVANCING EARTH AND SPACE SCIENCE

Geochemistry, Geophysics, Geosystems

RESEARCH ARTICLE
10.1029/2018GC007610

Key Points:
- Hydrothermal experiments were performed to extend the range of the Si-Cl geothermobarometer
- Vent fluids at the Piccard hydrothermal field, Mid-Cayman Rise, reach 540 °C, 62.5 MPa in the subsurface
- The Si-Cl geothermobarometer provides important pressure-temperature constraints to accurately calculate heat and mass fluxes

Supporting Information:
- Supporting Information S1

Correspondence to:
C. Tan,
tanc@umn.edu

Citation:
Scheuermann, P. P., Tan, C., & Seyfried, W. E., Jr. (2018). Quartz solubility in the two-phase region of the NaCl-H_2O system: An experimental study with application to the Piccard hydrothermal field, Mid-Cayman Rise. *Geochemistry, Geophysics, Geosystems*, *19*, 3570–3582. https://doi.org/10.1029/2018GC007610

Received 11 APR 2018
Accepted 4 SEP 2018
Accepted article online 11 SEP 2018
Published online 28 SEP 2018

Quartz Solubility in the Two-Phase Region of the NaCl-H_2O System: An Experimental Study With Application to the Piccard Hydrothermal Field, Mid-Cayman Rise

Peter P. Scheuermann[1], Chunyang Tan[1], and William E. Seyfried Jr.[1]

[1]Department of Earth Sciences, University of Minnesota, Minneapolis, MN, USA

Abstract Hydrothermal experiments were performed at elevated temperature (420–500 °C) and pressure (31.0–51.0 MPa) in the NaCl-H_2O system to measure quartz solubility in coexisting vapor and liquid and extend the calibrated range of the Si-Cl geothermobarometer. In the vapor, the density-based equations for quartz solubility of Fournier (1983, http://doi.org/10.1016/0016-7037(83)90279-X) and Von Damm et al. (1991, http://doi.org/10.2475/ajs.291.10.977) agree well with the experimental data, while the equation of Fournier (1983) also accurately predicts $SiO_{2(aq)}$ concentrations in the liquid. Importantly, the equations of Fournier (1983) and Von Damm et al. (1991) were calibrated based on quartz solubility in single phase fluids (no coexisting vapor-liquid) at higher pressure than investigated here. The new experimental data therefore extend the pressure range of the density-equations and demonstrate that quartz solubility in either vapor or liquid can be treated independently as a function of temperature, pressure, and fluid density. The Si-Cl geothermobarometer indicates that fluids venting from Piccard reach 540 ± 15 °C, 62.5 ± 3.0 MPa. These are the hottest and deepest conditions yet recorded by an actively venting seafloor hydrothermal fluid. Based on the calculated enthalpy differences between the subsurface fluid and that venting at the seafloor, approximately one third of the heat extracted at depth is lost during conductive cooling of the hydrothermal fluid. Incorporating the heat lost during conductive cooling into the overall budget at Piccard yields a flux of 100 ± 37 MW and an associated hydrothermal fluid flux of 1.2 ± 0.4 × 10^9 kg/year. The newly calibrated Si-Cl geothermobarometer provides important constraints for accurate determination of heat and mass fluxes at axial vent sites.

1. Introduction

Mid-ocean ridge (MOR) hydrothermal fluids play an important role in mass and heat transfer in the oceanic crust (Bischoff & Seyfried, 1978; Geiger et al., 2005; Lowell et al., 1995). In order to quantitatively understand the evolution of seafloor vent fluids, the phase equilibria of the bulk fluid (3.2 wt% NaCl) as well as minor components (e.g., Fe, $SiO_{2(aq)}$, and $H_{2(aq)}$) must be known at elevated temperature and pressure. Of particular interest are the high temperatures (>400 °C) and relatively low pressures (30–50 MPa) that occur at the magma-hydrothermal interface, because it is here that vent fluids most effectively react and equilibrate with the surrounding host rock before venting to the seafloor (German & Seyfried, 2014; Von Damm, 1995). Phase equilibria in the NaCl-H_2O system are now well constrained at all pressure-temperature conditions relevant to MOR vent systems due to numerous experimental studies carried out over several decades (Bischoff, 1991; Bischoff et al., 1986; Olander & Liander, 1950; Rosenbauer & Bischoff, 1987; Sourirajan & Kennedy, 1962). Quartz solubility has also been the target of numerous experimental studies given the high concentration of $SiO_{2(aq)}$ in many seafloor hydrothermal fluids (e.g., Bowers et al., 1988; Foustoukos & Seyfried, 2007; Von Damm, 1988; Von Damm et al., 1991).

The dissolution of quartz in pure water and NaCl-bearing fluids can be represented as a hydration reaction

$$SiO_{2(qtz)} + nH_2O = SiO_2{\cdot}nH_2O_{(aq)} \quad (1)$$

Equation (1) suggests that quartz solubility can be quantified as a function of the activity of water in addition to pressure and temperature (Fournier, 1983). In empirical formulations of quartz solubility, solution density is assumed to approximate water activity effects, even though this assumption is not yet grounded in a theoretical explanation (Akinfiev & Diamond, 2009). Using this approach, equations for quartz solubility have been calibrated in single-phase fluids (i.e., no coexisting vapor and liquid) over a wide range of temperatures,

pressures, and fluid compositions (Fournier, 1983; Fournier & Potter, 1982; Manning, 1994; Von Damm et al., 1991; Xie & Walther, 1993).

Quartz is ubiquitous in in situ sections of altered oceanic crust (Alt et al., 2010), ophiolite outcrops on land (Kelley et al., 1992; Richardson et al., 1987) and has recently been recovered from depth at the Reykjanes geothermal system (Friðleifsson et al., 2017). As a result, quartz has been inferred to control $SiO_{2(aq)}$ concentrations in coexisting aqueous fluids in active mafic-hosted hydrothermal systems. The pressure and temperature dependent nature of quartz solubility lends itself to application as a geothermobarometer in natural systems. Experimental quartz solubility data were first used to estimate the subsurface pressure-temperature conditions encountered by MOR vents fluids that had not undergone phase separation (Von Damm et al., 1991). However, phase separation of hydrothermal fluid is common in axial vent systems and the large physical and chemical differences between vapor, liquid, and single phase fluids result in markedly different quartz solubility in each fluid. Accordingly, Foustoukos and Seyfried (2007) measured quartz solubility in low-density vapors between 390 and 430 °C, 25.0–35.0 MPa, in keeping with apparent subsurface conditions in many basalt-hosted MOR hydrothermal systems. Quartz solubility in the vapor was emphasized since it is this low-density fluid that commonly vents at the seafloor, providing information on subsurface conditions. When combined with dissolved Cl concentrations, vapor phase quartz solubility allows for estimation of the subsurface pressure-temperature conditions encountered by fluids at basalt-hosted MOR hydrothermal vent systems (Fontaine et al., 2009). This method, known as the Si-Cl geothermobarometer, yields important information regarding the physical conditions at which mass transfers from the oceanic crust to hydrothermal fluids, with broader implications relevant to changes in the heat content of hydrothermal fluid during ascent to the seafloor.

The recently discovered Piccard hydrothermal field lies at a depth of 4,960 m below sea level on the Mid-Cayman Rise (Connelly et al., 2012) and is the deepest known high temperature hydrothermal vent system (German, Bowen, et al., 2010). Due to the extreme depth, maximum vent fluid exit temperatures reach 398 °C (McDermott et al., 2018). Surprisingly, dissolved Cl concentrations are depleted relative to seawater, indicating phase separation occurring in the subsurface, the high hydrostatic pressure notwithstanding. Based on the depth of the vent field, fluids venting at Piccard must reach at least 483 °C in order to intersect the two phase boundary for seawater (Bischoff & Pitzer, 1989; McDermott et al., 2018). The subsurface pressure temperature conditions at the Piccard vent field are therefore well outside the current range (390–430 °C) of calibrated vapor-phase quartz solubility.

In the present study, quartz solubility in low-chlorinity vapors was determined experimentally from 420 to 500 °C, 31.0–51.0 MPa. Samples of the coexisting liquid phase were also taken along the 420 °C isotherm to determine $SiO_{2(aq)}$ partitioning between fluid phases. Experiments were performed in a newly constructed fixed volume titanium reactor that allows for excellent control of pressure, temperature, and fluid composition. The experimental data are compared with equations that express quartz solubility as a function of pressure, temperature, and fluid density. The good agreement between density equations and experimental data allows the density equations to be used in combination with Cl solubility to estimate the subsurface pressure-temperature conditions at the Piccard hydrothermal site. Heat and mass transfer fluxes at Piccard show considerable difference when calculated based on subsurface pressure–temperature conditions as compared to those calculated using seafloor conditions.

2. Methods

2.1. Hydrothermal Reactor

Experiments were performed in a newly designed fixed volume hydrothermal reactor (Figure 1). The internal volume of the reactor is 150 mL. The body and closure piece are constructed from Ti-6Al-2Sn-4Zr-2Mo (Ti6242), a high strength titanium alloy, while 1/16″ (all diameters reported are measurements of outer diameter) capillary lines and high temperature adapters are made from grade 2 titanium. The angle of the closure piece differs by 2° from that of the body of the reactor to form a cone seal. To our knowledge, this is the first cone seal hydrothermal reactor capable of reaching 51.0 MPa at temperatures up to 500 °C. To reinforce the cone seal, a stainless steel thrust washer sits between the closure piece and main nut. The greater thermal expansion of steel relative to titanium ensures evenly distributed force is applied

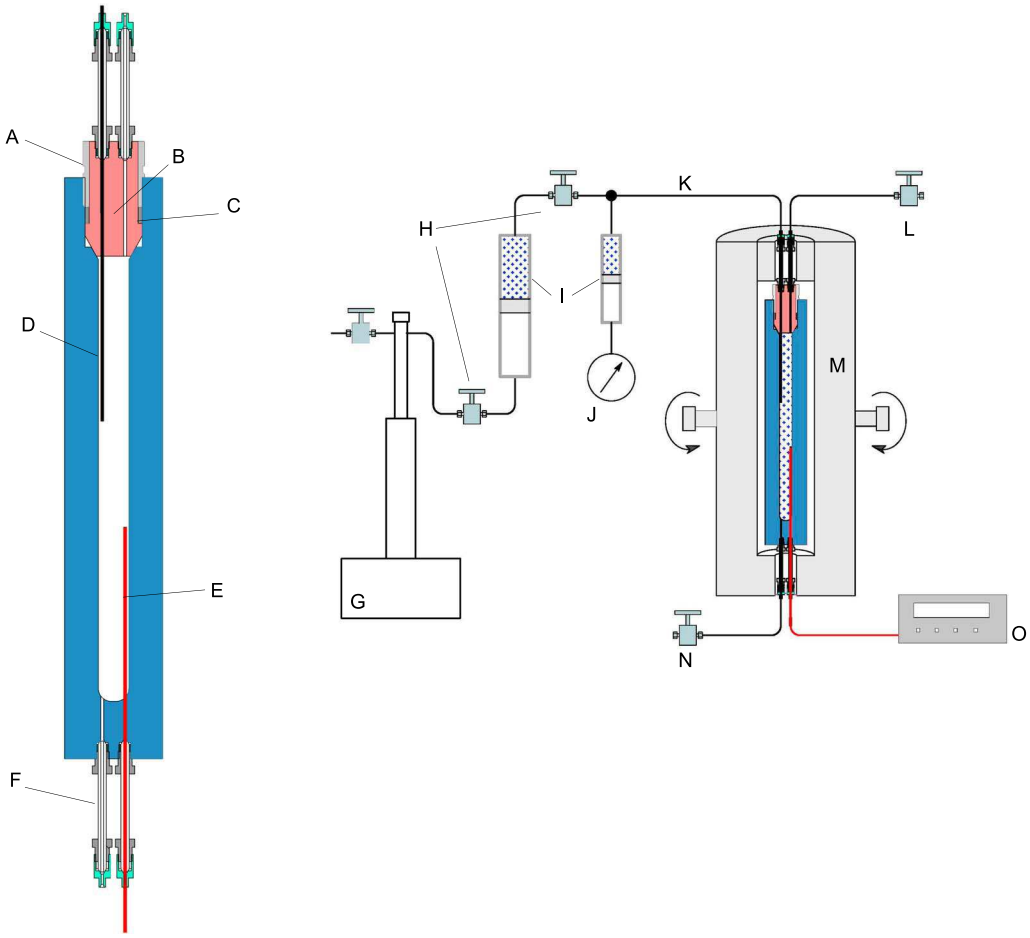

Figure 1. Drawings of the newly designed hydrothermal reactor and the experimental set up. (a) Main nut, (b) closure piece, (c) stainless steel thrust washer, (d) capillary tubing for injecting fresh experimental solution, (e) thermocouple, (f) titanium adapter, (g) Teledyne Isco syringe pump, (h) check valves, (i) titanium piston separators, (j) Heise pressure gauge, (k) 1/16″ titanium tubing, (l) vapor sampling valve, (m) calc-silicate furnace, (n) liquid sampling valve, and (o) temperature control panel.

to the cone seal from above (Shmulovich et al., 1995). The adapters also form cone seals with the reactor and are larger (1/4″) than those used on previous fixed volume reactors constructed in our laboratory. Extended periods at elevated temperature causes titanium to deform and seize to adjoining surfaces. The cone seal and larger size of the adapters minimizes deformation and facilitates removal upon completion of an experiment.

A 1/16″ Ti-sheathed type E (chromel-constantan) thermocouple monitors the fluid temperature inside the reactor. The thermocouple communicates with three external heating bands through an EZ Zone PM (Watlow Electric Manufacturing Co.) proportional-integral-derivative controller. The heating bands attach to the outside of a steel cylinder that holds the reactor. The reactor, heating bands, and steel cylinder are housed in a calcium-silicate furnace, and void space is filled with a ceramic fiber blanket (Pester et al., 2015). The furnace is attached to a steel frame and can rotate to promote mixing (Seyfried et al., 1987).

A Teledyne ISCO syringe pump controls the system pressure, up to a maximum of 51.7 MPa. The syringe pump is particularly useful in that it can automatically inject or withdraw fluid to maintain constant pressure during sampling, and move between any two pressure conditions. A titanium piston separator is positioned between the syringe pump and reactor to prevent corrosive experimental solution from damaging the syringe pump. To record any pressure differential across the piston, a digital pressure gauge (Heise® ST-2H) is situated between the reactor and separator. A smaller piston separator protects the Heise gauge from

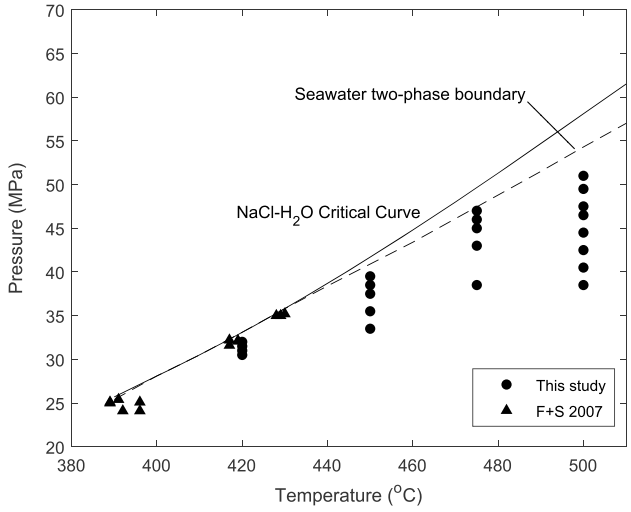

Figure 2. Pressure temperature conditions at which samples were taken during the current study and Foustoukos and Seyfried (2007). Also shown for reference are the NaCl-H_2O critical curve (solid line) and the boiling curve of seawater (dashed line), 3.2 wt% NaCl (Driesner, 2007).

corrosive fluid. During the present experiments, the pressure difference between the ISCO pump and Heise gauge never exceeded 0.5 MPa, with the ISCO pump always recording the higher pressure.

At both ends of the reactor, the capillary lines connect to high pressure titanium metering valves (Parker Autoclave Engineers) through which fluid samples are taken. Two additional titanium valves, between the reactor and piston separator, allow the experimental solution in the separator to be changed while maintaining elevated pressure within the reactor. The bulk chemistry of the experiment can therefore be modified by injection of new experimental solution.

2.2. Experimental Procedure

Before each experiment, the thermocouple was calibrated at experimental temperatures using a dry block probe calibrator (Omega Hot Point®) and always recorded within 3 °C of the calibrator set point. Blue Moly, an anti-seize compound, was applied to all metal surfaces that do not come in contact with the fluid. The main seal and four high temperature adapters were closed with 180 and 20 ft·lb, respectively.

The quartz grains used in the experiments were approximately 200 μm long and were placed in an open 5 × 3 cm gold capsule at the bottom of the reactor. Visibly clear quartz crystals were obtained from the University of Minnesota mineral collection. The purity of the crystals was confirmed by X-ray diffraction and inductively coupled plasma optical emission spectroscopy (ICP-OES) analysis. The starting experimental solutions varied between 0.55–1 mol/$kg_{solution}$ NaCl, acidified to $pH_{25\ °C}$ 2.5–3.75 with concentrated, trace metal grade HCl. Approximately 1 mmol HCl was required to acidify the starting solutions.

Experiments were performed isothermally and the pressure began at the lowest condition and was increased after each sample extraction (Figure 2). The pressure reported for each sample is that recorded by the Heise gauge. Once at the appropriate pressure and temperature, the entire system was allowed to react for 48 hours at 420, 450, and 475 °C and 24 hours at 500 °C to achieve equilibrium, consistent with previously determined time constraints on quartz-fluid equilibrium at similar temperature conditions (Xie & Walther, 1993). These reaction times were also confirmed by reversing equilibrium through temperature adjustment and measuring $SiO_{2(aq)}$ concentrations. Reproducible results were achievable without rocking the autoclave, so for simplicity, the autoclave was positioned at a slight angle above horizontal. This angle promoted segregation of vapor and liquid that were then sampled from opposite ends of the reactor. Prior to sampling, approximately 0.3 g of fluid were removed to flush the capillary line. Each sample weighed between 1–2 g and was collected in a clean luer lock syringe. Aliquots for $SiO_{2(aq)}$ were diluted at least 20-fold with 1 mL 1 M Optima HCl and sufficient 18.2 mΩ deionized water immediately after sampling (Foustoukos & Seyfried, 2007; Von Damm et al., 1991). Additional aliquots were also taken to determine Na and Cl concentrations and $pH_{25\ °C}$.

2.3. Analytical Methods

Na was measured by ICP-OES, while Cl was measured by ion chromatography (IC). Samples measured by ICP-OES were analyzed three times and those measured by IC were run twice. The average of these values is reported. Uncertainties for the ICP-OES and IC are 3% and 2%, respectively (2σ, Table 1). The concentration of $SiO_{2(aq)}$ in all samples was measured using the molybdate blue method (Hansen & Koroleff, 1999), with an associated uncertainty of 5% (2σ). Additionally, 10 samples were analyzed for $SiO_{2(aq)}$ using ICP-OES. With one exception (sample 12), the difference between spectrophotometric and ICP-OES measurements was less than 10%. $pH_{25\ °C}$ was measured using a Thermo-Ross electrode that was calibrated with pH 4, 7, and 10 buffers before each measurement.

2.4. Calculation of Quartz Solubility and Vapor-Liquid Partitioning

Quartz solubility was calculated using the density equations of Fournier (1983), Von Damm et al. (1991), Foustoukos and Seyfried (2007), and Akinfiev and Diamond (2009). The density of NaCl-H_2O fluids was

Table 1
Chemical Composition of Fluid Samples

Sample	T (°C)	Pressure (MPa)	Phase	SiO_2 (Spec)	SiO_2 (ICP-OES)	Na	Cl	$pH_{25\ °C}$
1	420	32.5	vapor	12.00			565	3.11
2	420	32.5	liquid	20.15			1,413	3.17
3	420	32.0	vapor	6.55			163	2.91
4	420	32.0	liquid	20.89			1,893	3.28
5	420	31.5	vapor	5.82			115	3.04
6	420	31.5	liquid	21.75			1,967	3.19
7	420	31.0	vapor	4.77			76	2.75
8	420	31.0	liquid	21.42			2,313	3.1
9	450	400	vapor	11.35			396	2.85
10	450	39.5	vapor	10.40	10.10		275	3.29
11	450	38.5	vapor	8.36			179	2.64
12	450	37.5	vapor	6.20	5.40		131	3.33
13	450	35.5	vapor	5.81	5.60		67	3.18
14	450	33.5	vapor	3.86			41	2.61
15	475	47.0	vapor	14.33			475	3.7
16	475	46.5	vapor	12.44			345	
17	475	46.0	vapor	12.30			315	2.74
18	475	44.5	vapor	10.50	10.10		205	3.09
19	475	43.0	vapor	8.30	7.90		140	3.01
20	475	38.5	vapor	5.05			53	2.6
21	500	51.0	vapor	12.55			237	2.58
22	500	49.5	vapor	11.41			182	2.66
23	500	47.5	vapor	10.23			175	2.65
24	500	46.5	vapor	9.22	9.51	112		2.62
25	500	44.5	vapor	7.64	7.72	75		2.58
26	500	42.5	vapor	6.93	6.98	55		2.48
27	500	40.5	vapor	5.30	5.20	37		2.38
28	500	38.5	vapor	5.04	5.10	28		2.52

Note. All concentrations are $mmol/kg_{solution}$. %RSD for Na, Cl, and SiO_2 are 3, 2, and 5 (2σ), respectively. SiO_2 (spec) refers to samples analyzed on a spectrophotometer using the molybdate blue method. SiO_2 (ICP-OES) refers to samples analyzed with ICP-OES. [Na] = [Cl], within error. ICP-OES = inductively coupled plasma optical emission spectroscopy.

calculated using the equations of Driesner (2007) and the International Association for the Properties of Water and Steam 1995 (IAPWS95) formulation for pure water (Wagner & Pruss, 2002). All calculations were performed in MATLAB using WATER95 (Junglas, 2009).

In their contribution, Akinfiev and Diamond (2009) set the molar volume of liquid NaCl at 30.8 cm^3/mol regardless of the pressure and temperature condition. In the present study, no appreciable differences in quartz solubility predictions were noticed between results using the fixed molar volume or when molar volume was calculated as a function of pressure and temperature using the correlations of Driesner (2007). When calculating quartz solubility using the equation of Fournier (1983) the density correction due to waters of hydration was considered to be negligible. No changes were made to the equations of Von Damm et al. (1991) or Foustoukos and Seyfried (2007).

In keeping with previous studies (Pokrovski et al., 2005; Styrikovich et al., 1955), $SiO_{2(aq)}$ partitioning between coexisting vapor and liquid is defined as

$$K_D = m_{vap}/m_{liq} \tag{2}$$

$$\text{Log } K_D = n \times \log\left(\rho_{vap}/\rho_{liq}\right) \tag{3}$$

where m is the molar concentration ($mmol/kg_{solution}$), ρ is density (g/cm^3), and *n* represents an empirical regression coefficient that reflects the extent of vapor-phase hydration and species volatility (Palmer & Simonson, 1996). Larger values of *n* indicate increased partitioning into the vapor phase (Palmer & Simonson, 1996).

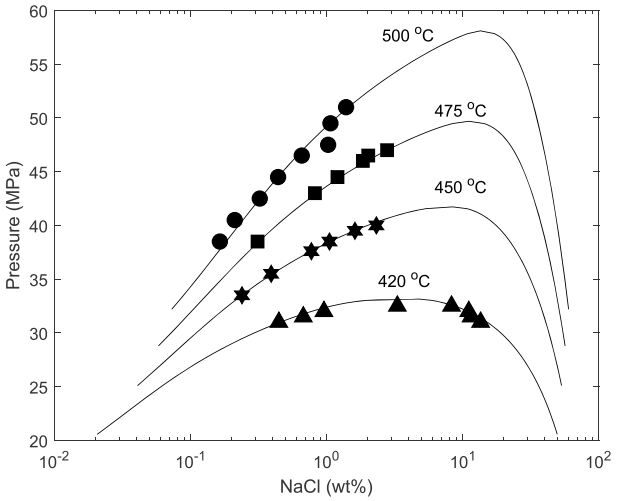

Figure 3. NaCl composition of all samples plotted against the predicted isotherms (solid lines) of Driesner (2007) and Driesner and Heinrich (2007). NaCl concentrations are taken as equal to either Cl or Na. The good agreement between experimental data and model isotherms suggest the bulk matrix achieved chemical equilibrium and highlights the accuracy of the experimental pressure-temperature system.

3. Results

NaCl concentrations from the present study (vapor-liquid coexistence) agree well with predictions based on the numerical model of Driesner (2007) and Driesner and Heinrich (2007) and indicate equilibrium conditions for the NaCl-H_2O system (Figure 3). The good agreement also demonstrates that any pressure differentials across the smaller piston separator were negligible.

$SiO_{2(aq)}$ concentrations in the vapor display a clear dependence on temperature and Cl concentration (Figure 4a and Table 1). For a given Cl concentration, $SiO_{2(aq)}$ increases with increasing temperature and along each isotherm $SiO_{2(aq)}$ concentrations increase as a logarithmic function of Cl concentration (i.e., density). In the liquid phase, quartz solubility exhibits less of a dependence on Cl concentration (Figure 4b). Liquid samples were not taken at 450, 475, and 500 °C since the high dissolved NaCl concentrations at these temperatures would have precipitated halite in the lower temperature capillary tube upon sampling.

The value for n (equation (3)) regressed from the experimental data is 1.38 ± 0.1 (Figure 5). The density of each sample was calculated using the equations discussed in section 2.4 and the measured temperature, pressure, and dissolved Cl concentration. At similar pressure-temperature-composition conditions, other workers have calculated n to be 2.01 (Pokrovski et al., 2005) and 1.79 (Von Damm et al., 1991).

4. Discussion

4.1. Comparison of Measured and Calculated Quartz Solubility in Coexisting Vapor and Liquid

Experimental data from the current study are compared with the density equations for quartz solubility of Fournier (1983), Von Damm et al. (1991), Akinfiev and Diamond (2009), and Foustoukos and Seyfried (2007; Figure 6) to assess whether these equations are applicable to pressure-temperature conditions relevant to MOR vent systems. Only a brief description of each model as it relates to the experimental data from the current study is presented.

The good agreement between the equation of Von Damm et al. (1991) and the present experimental data in the vapor stems from the generally similar pressure-temperature-composition conditions investigated. Von Damm et al. (1991) regressed their equation based on 494 quartz solubility measurements in pure water, 0.5 M NaCl and 0.55 M NaCl, from 25 to 900 °C and 0.1–1,000 MPa. Statistical regression of such a large data set can account for the effects of temperature, pressure, density, and NaCl concentration within the empirically derived coefficients. The empirical nature of the Von Damm et al. (1991) equation can be seen in the poor agreement with the experimental data in the liquid phase, which contains much higher NaCl concentrations than used in the original regression (Figure 7).

Fournier (1983) modified an earlier regression of quartz solubility in pure water (Fournier & Potter, 1982) to account for the effects of NaCl by substituting the effective density for the density of pure water. This substitution assumes that the effective density approximates the activity of water, which plays an important role in determining quartz solubility (equation (1); Fournier, 1983). The equation of Fournier (1983) reproduces experimental data from both coexisting vapor and liquid phases well (Figures 6 and 7). While still empirically derived, the success of the Fournier (1983) equation in reproducing the new experimental data suggests the underlying assumptions are valid in the SiO_2-H_2O-NaCl system.

Akinfiev and Diamond (2009) expanded on the work of Fournier (1983) by expressing quartz solubility in the NaCl-CO_2-H_2O system as a function of the effective molar volume of water and the mole fraction of water. This equation slightly underestimates quartz solubility at all conditions in the current study, but accurately reproduces the trends with fluid density in both the vapor and liquid (Figures 6 and 7). As noted by the authors, small inaccuracies are acceptable if their equation reproduces well the overall

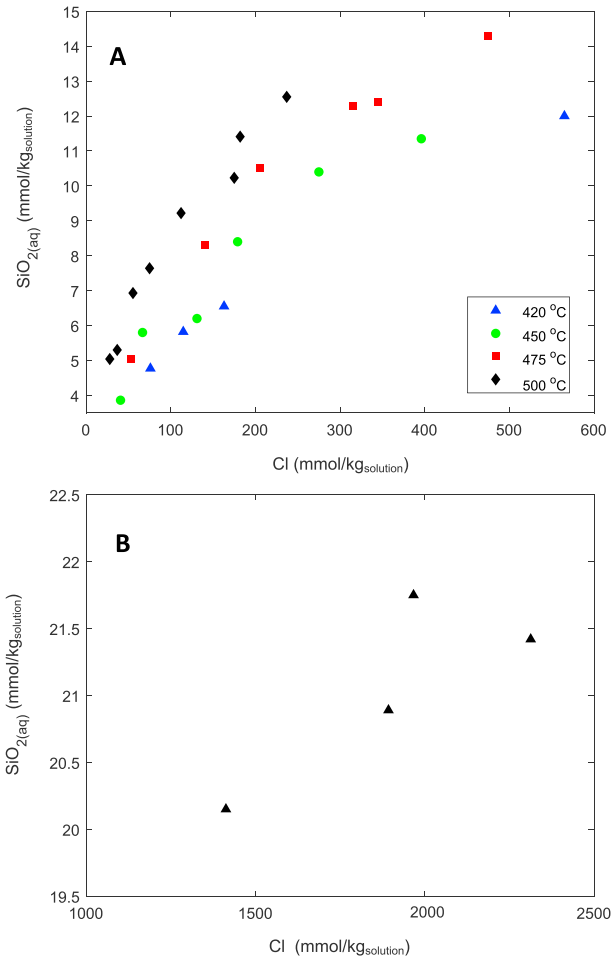

Figure 4. (a) Quartz solubility in the vapor as a function of temperature and dissolved Cl concentration. Greater Cl concentrations indicate higher pressures along a given isotherm, as dictated by phase relations in the NaCl-H_2O system. (b) Quartz solubility in the liquid at 420 °C as a function of Cl concentration. In the liquid phase, greater Cl concentrations indicate decreasing pressure.

solubility trend allowing quartz solubility to be semiquantitatively determined in regions beyond current experimental calibration (Akinfiev & Diamond, 2009). Substitution of the *n* value calculated in the present study, 1.38, results in only minor improvement in agreement between the calculated and experimental quartz solubility. This result indicates that the *n* value as determined here may have physical meaning, but the waters of hydration do not play a significant role in controlling quartz solubility at the experimental conditions (Fournier, 1983).

All density equations described above are based on quartz solubility in single phase fluid systems (i.e., no coexistence of vapor and liquid). The generally good agreement between these equations and quartz solubility generated in the present study (two distinct fluid phases) confirms that quartz solubility in either fluid can be treated individually; partitioning between coexisting fluids need not be taken into account. Quartz sets the activity of $SiO_{2(aq)}$ equal in both phases and differences in NaCl concentrations and density result in varying $SiO_{2(aq)}$ concentrations. While there is currently no strong theoretical link between density and thermodynamic properties of aqueous solutes, the correlation between the dielectric constant and density of water (Dolejs, 2013) may explain the success of the density models. Numerous studies have shown that the dielectric constant of water plays a key role in the calculation of the thermodynamic properties of aqueous solutes at a wide range of pressure-temperature conditions (e.g., Helgeson & Kirkham, 1974; Sverjensky et al., 2014).

Similar to the present study, the quartz solubility data of Foustoukos and Seyfried (2007) were measured in low-density vapor between 390 and 430 °C. The two data sets show relatively good agreement at 420 °C (Figure 6a). However, quartz solubility as determined by Foustoukos and Seyfried (2007) does not increase as significantly with dissolved Cl concentration as reported here. Additionally, due to the experimental design, it was difficult for these authors to perform experiments at pressure conditions far removed from the critical curve of the NaCl-H_2O system (Figure 2; Foustoukos & Seyfried, 2007). These issues result in regression of an equation that overestimates quartz solubility outside the calibrated range (Figure 6, 450 °C).

4.2. Si-Cl Geothermobarometry: Application to the Piccard Hydrothermal Field, Mid-Cayman Rise

The chemistry of the buoyant Piccard plume as well as the seafloor geology provide evidence that hydrothermal fluid circulation at Piccard involves interaction with mafic lithologies. German, Bowen, et al. (2010) report CH_4/Mn ratios in the Piccard plume that are similar to those found above well-studied mafic-hosted vent systems such as East Pacific Rise (9°50′N) and TAG (26°N MAR) and are easily distinguishable from those emanating from the ultramafic hosted Rainbow vent site. Consistent with plume chemistry, Hayman et al. (2011) and Elthon et al. (1995) collected predominantly basalt and gabbro along the bottom of the axial trough in which the Piccard site is located. Along the walls of the axial trough other researchers have reported gabbro with minor amounts (~15%) of ultramafic rocks (Ito & Anderson, 1983; Stroup & Fox, 1981). The presence of ultramafic lithologies is manifest in the plume and fluid chemistry of the Europa and Walsh vent sites, both of which are significantly different than at Piccard (German, Bowen, et al., 2010). Based on analysis of dredged rock samples and magnetic data, Stroup and Fox (1981) and Hayman et al. (2011) proposed an oceanic core complex model for the Mid-Cayman Rise. In this model a thin layer (several hundred meters) of diabase and basalt are underlain by 1–2 km of gabbro. Ultramafic lithologies exist along crustal faults (Stroup & Fox, 1981).

In keeping with previous studies (Bowers et al., 1988; Fontaine et al., 2009; Von Damm et al., 1991), the mafic crust at Piccard allows for application of the Si-Cl geothermobarometer. This method takes

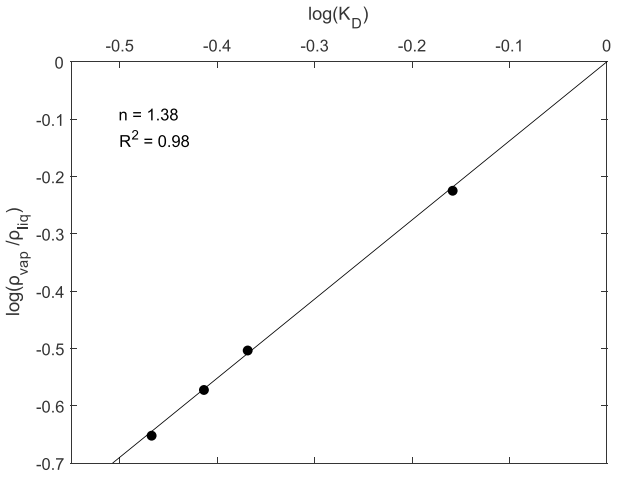

Figure 5. Graphical representation of $SiO_{2(aq)}$ vapor-liquid partitioning. The slope of the linear regression represents the *n* value, which describes the volatility of $SiO_{2(aq)}$. See section 2.4.

advantage of the pressure-temperature dependent solubility of both quartz and Cl in the two phase region of the NaCl-H_2O system (Fontaine et al., 2009). At a given pressure-temperature condition within the vapor-liquid region of the NaCl-H_2O system, the NaCl composition, and therefore density, of both the vapor and liquid are invariant (Liebscher & Heinrich, 2007). The density, in turn, fixes quartz solubility. Unique subsurface conditions can then be calculated using measured concentrations of $SiO_{2(aq)}$ and Cl in vent fluid samples. In addition to the presence of quartz, the Si-Cl method relies on the assumption that $SiO_{2(aq)}$ and Cl concentrations equilibrate at the moment of fluid phase separation and remain constant during ascent to the seafloor. Cl has been shown to be conservative in MOR fluids (e.g., German & Seyfried, 2014). With respect to the Piccard field, measured concentrations of Ca, $H_{2(aq)}$, $H_2S_{(aq)}$, and Fe are notably different than measured at lower temperature mafic-hosted systems (e.g., Foustoukos et al., 2009; Pester et al., 2011; Von Damm, 1995) providing strong evidence that these fluids record the chemical signature of extremely high temperature-pressure reactions (McDermott et al., 2018).

End-member vent fluids from the Piccard Vent field demonstrate a narrow range of $SiO_{2(aq)}$ (18.9–20.3 mmol/$kg_{solution}$) and Cl (342–352 mmol/$kg_{solution}$) concentrations (McDermott et al., 2018). Given the similarity in composition between individual vents, an average end-member concentration for the entire site can be calculated, 20 mmol/$kg_{solution}$ $SiO_{2(aq)}$ and 350 mmol/$kg_{solution}$ Cl (McDermott et al., 2018). The quartz solubility equations of Von Damm et al. (1991) and Fournier (1983) are used with Cl solubility as calculated by Driesner and Heinrich (2007).

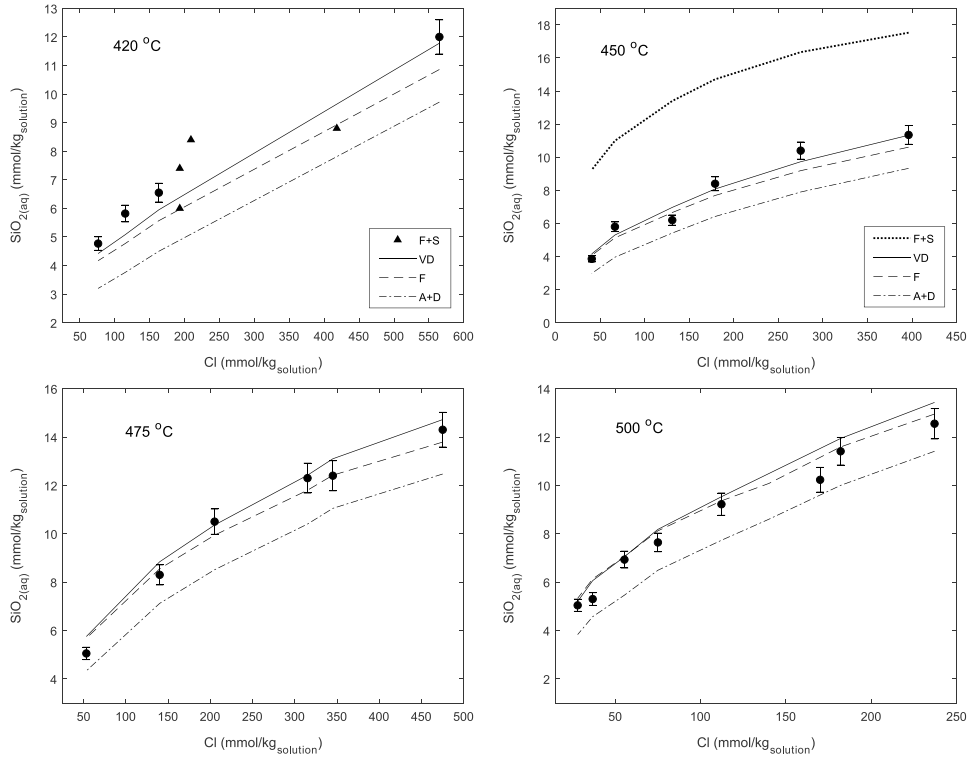

Figure 6. Experimental quartz solubility in the vapor (circles, this study; triangles, Foustoukos & Seyfried, 2007) as compared to the density equations of Von Damm et al. (1991), Fournier (1983), Akinfiev and Diamond (2009), and Foustoukos and Seyfried (2007). The equations of Von Damm et al. (1991) and Fournier (1983) accurately recreate the experimental data while the equations of Akinfiev and Diamond (2009) and Foustoukos and Seyfried (2007) underestimate and overestimate, respectively, quartz solubility at the experimental conditions. See Table 1 for associated pressures.

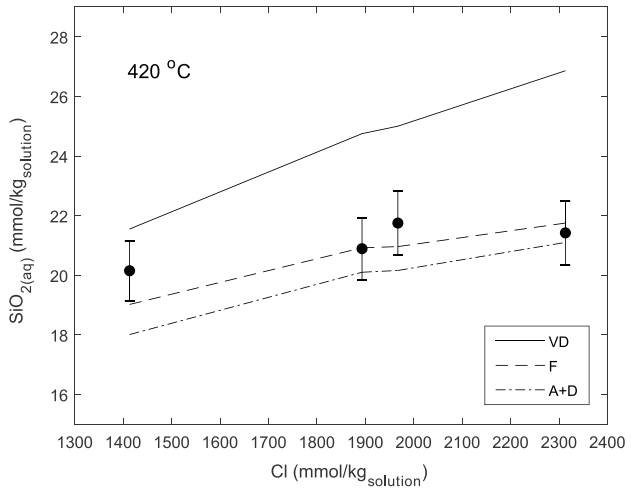

Figure 7. Experimental quartz solubility in the liquid compared to density based equations. The equation of Fournier (1983) best recreates the experimental data, while the equation of Von Damm et al. (1991) significantly overestimates quartz solubility. See section 4.1 for further discussion.

The Si-Cl geothermobarometer yields subsurface temperature and pressure conditions of 540 ± 15 °C, 62.5 ± 3.0 MPa for fluids issuing from the Piccard vent field (Figure 8). Uncertainties are based on the largest difference, 1.2 mmol/$kg_{solution}$ $SiO_{2(aq)}$, between density equations and experimental data. The estimated subsurface pressure-temperature conditions at Piccard are the hottest and deepest reflected by any active MOR hydrothermal fluid. Assuming cold hydrostatic pressure, the calculated pressure indicates fluids circulate to approximately 1,200 m below the seafloor. Br/Cl ratios in the Piccard fluids indicate phase separation occurs between 555–573 °C, 60.0 MPa (McDermott et al., 2018), in good agreement with the Si-Cl estimate presented here.

4.3. Heat and Mass Fluxes at Piccard

Quantification of the physical conditions at which hydrothermal alteration occurs provides constraints necessary to interpret heat and mass transfer fluxes at Piccard, with broader implications for the global MOR system. Previous studies of individual vent sites have calculated hydrothermal heat flux by measurement of temperature and flow rate directly at the vent orifice or by measurement of the physical characteristics of the hydrothermal plume (e.g., German, Thurnherr, et al., 2010; Germanovich et al., 2015). In effect, these studies calculate the heat that reaches the overlying water column but do not include heat lost by conductive cooling of source fluids in the ocean crust during ascent to the seafloor. Conductive cooling of vent fluids has long been recognized at MOR vent sites (Berndt et al., 1989), but without accurate estimates of subsurface pressure and temperature the amount of heat transferred back to the crust is difficult to quantify. Here we calculate the hydrothermal heat flux at Piccard as a combination of the heat lost to the overlying water column and, as a result of the Si-Cl results, we are able to incorporate the heat lost during conductive cooling.

The height of the buoyant plume at Piccard can be used as a proxy to estimate heat flux entering the water column (Little et al., 1987). Conductivity-temperature-depth data taken from the water column above the Piccard site indicate that the buoyant plume rises to a water depth of at least 3,950 m, or 1,010 m above the black smoker chimneys (German, Bowen, et al., 2010). However, as emphasized by Rudnicki and German (2002), plume heights can vary with time. Estapa et al. (2015) place the maximum plume height at approximately 4,100 m depth, 150 m below the value of German, Bowen, et al. (2010), although it is possible that the plume rises higher than this given the apparent uncertainties. To compensate for changes in the maximum height, we use 3,950 ± 150 m as the top of the Piccard plume. Using simple plume theory (Fischer et al., 1979; Little et al., 1987), the heat flux entering the ocean is estimated to be 75 ± 37 MW (supporting information).

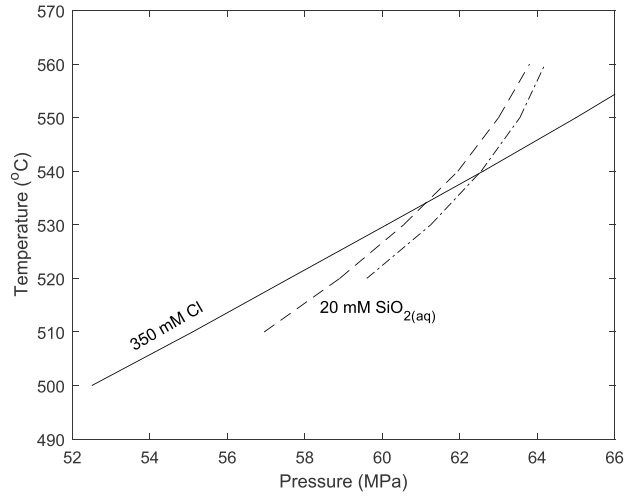

Figure 8. The Si-Cl geothermobarometer as applied to the Piccard vent field, Mid-Cayman Rise. The end-member hydrothermal fluid at Piccard contains 350 mmol/$kg_{solution}$ Cl and 20 mmol/$kg_{solution}$ $SiO_{2(aq)}$. Cl concentration as calculated by Driesner and Heinrich (2007), while $SiO_{2(aq)}$ is calculated using the equations of Von Damm et al. (1991; dashed line) and Fournier (1983; dash-dot). The intersection of the Cl and $SiO_{2(aq)}$ isoconcentration lines yield the subsurface pressure–temperature conditions, 540 ± 15 °C, 62.5 ± 3.0 MPa.

The hydrothermal heat lost during conductive cooling can be calculated as the difference in the enthalpy of the fluid at depth in the ocean crust and the enthalpy when venting at the seafloor. Using equations from Driesner (2007), the fluid enthalpy at depth is 2,775 J/g, while at the seafloor the enthalpy decreases to 1,818 J/g (Table 2). The fluid therefore loses 957 J/g, or approximately one third of the total heat extracted at depth. Adding the proportion of heat lost during conductive cooling (one third of 75 MW) into the plume calculated flux results in a total hydrothermal heat flux of 100 ± 37 MW (supporting information).

Previous work has suggested that the majority of heat that leaves the ridge axis is carried not by high-temperature fluids but instead by low temperature diffuse flow fluids (Elderfield & Schultz, 1996; Nielsen et al., 2006; Schultz et al., 1992; Veirs et al., 2006). At Piccard, the chemistry of the diffuse fluids represents a mix of cold seawater and end member

Table 2
Values Used to Calculate Heat and Mass Fluxes

	Seafloor	Subsurface
Pressure (MPa)	49.6	62.5
Hydrothermal fluid temperature (°C)	398	540
ΔT^a	393	535
Cl concentration ($mmol/kg_{sol'n}$)	350	350
Enthalpy (J/g)	1818	2,775
C_p ($J\ kg^{-1}\ K^{-1}$)	4.47×10^3	4.97×10^3
Heat flux[b] (MW)	75	100

Note. Bottom seawater temperature (5 °C) measured by McDermott et al. (2018). Subsurface heat flux incorporates the heat lost during conductive cooling into the overall hydrothermal heat budget.
[a]Temperature difference between hydrothermal fluid and bottom seawater. [b]Seafloor heat flux refers to that calculated using only the hydrothermal plume.

hydrothermal fluid (McDermott, 2015). This implies that the heat carried by diffuse flow fluids results from mixing with hot hydrothermal fluids. By calculating the enthalpy of the end-member hydrothermal fluid at depth, the heat flux presented here combines the two types of heat fluxes (diffuse and focused) observed at the seafloor.

The Piccard heat flux is considerably less than the average hydrothermal heat flux measured at individual sites along slow spreading ridges, 1,669 ± 1,354 MW, and is on the low end of heat fluxes measured along fast spreading centers, 245 ± 170 MW (Baker, 2007). The apparent discrepancy between the Piccard site and other slow spreading sites likely results from the extremely thin crust, 2–3 km (ten Brink et al., 2002), and relatively shallow subsurface fluid circulation at Piccard. Heat supply increases with crustal thickness, while the depth of fluid circulation determines the amount of heat available to hydrothermal fluids (Mottl, 2003). At slow spreading ridges, fluid circulation may reach to the base of the oceanic crust, 6–8 km below the seafloor (de Martin et al., 2007). Fluid circulation at fast spreading centers extends only 1–4 km below the seafloor due to shallow magma chambers that prevent deeper circulation (Canales et al., 2005; Detrick et al., 1987; Kent et al., 1993). Given the similarity in heat fluxes and depth of fluid circulation at Piccard and fast spreading vent sites it is likely a shallow magma chamber exists beneath Piccard. Kinsey and German (2013) calculate that a relatively small amount of magma, 1.6×10^9 m^3, is necessary to sustain high temperature fluid flow at Piccard.

Heat flux is necessary in order to determine the flux of hydrothermal fluid and associated geochemical components. The mass flux of hydrothermal fluid, F, can be calculated as

$$F = H/(C_p \Delta T) \tag{4}$$

where H is the heat flux (W), C_p is the heat capacity (constant pressure) of seawater ($J\ kg^{-1}\ K^{-1}$), and ΔT is the temperature difference between bottom seawater and hydrothermal temperatures (Elderfield & Schultz, 1996). Using a total heat output of 100 MW, a temperature averaged C_p (50 °C increments from 5 to 540 °C, 62.5 MPa) of 4.97×10^3 $J\ kg^{-1}\ K^{-1}$, and 535 K (Table 2) yields a mass flux of water of 1.2×10^9 kg/year at Piccard. Both terms in the denominator of equation (4) refer to subsurface conditions. Miscalculation of the fluid flux would arise if the heat emanating from the diffuse flow sites at Piccard were incorporated into the total heat flux without knowledge of subsurface conditions. In this case the total heat flux would approach 100 MW, yet C_p and ΔT would be calculated based on seafloor conditions. The fluid flux would then become 1.8×10^9 kg/year, or 50% greater than the original estimate of 1.2×10^9 kg/year.

In contrast to equation (4), heat flux can be calculated if fluid and geochemical fluxes are measured or estimated. This approach commonly uses the ^{3}He/heat ratio

$$^3He/heat = {}^3He/(C_p D\theta) \tag{5}$$

where ^{3}He represents concentration and $D\theta$ is the source temperature anomaly, analogous to ΔT (German, Thurnherr, et al., 2010; Jean-Baptiste et al., 2004). It is clear that accurate values for C_p and $D\theta$ are necessary to calculate source fluid ^{3}He/heat ratios. At Piccard, the ^{3}He concentration is 3.99×10^{-5} μM (McDermott, 2015) and the ^{3}He/heat ratio calculated using seafloor conditions is 50% greater than that calculated based on subsurface conditions.

The calculations presented here highlight the importance of incorporating subsurface pressure–temperature conditions when determining heat and mass fluxes at individual vent sites. Estimates of MOR hydrothermal heat fluxes based solely on seafloor conditions likely underestimate the true heat flux, since the hydrothermal heat budget of a vent system includes all heat that is available to drive fluid circulation (Mottl, 2003). How much heat is lost due to conductive cooling at a specific vent site will vary, but the results from Piccard show that the percentage of the total can be significant. It is important to remember that the Si-Cl method estimates the pressure-temperature conditions of fluid-rock chemical equilibrium, but not necessarily the maximum temperature reached by the fluids. The amount of heat lost to conductive cooling as calculated by Si-Cl

should therefore be viewed as a minimum in some cases. At some vent sites, such as EPR 9°50′N, the depth to the magma chamber is well constrained and in good agreement with Si-Cl estimates (Fontaine et al., 2009). Si-Cl pressure-temperature estimates at EPR 9°50′N likely capture the hottest and deepest conditions since fluid circulation below the magma chamber is unlikely. While Si-Cl pressure-temperature estimates do not capture the entire hydrothermal heat budget at all vent sites, the newly calibrated Si-Cl geothermobarometer provides an important improvement in quantifying heat and mass fluxes as compared to calculations based on seafloor conditions.

5. Summary

A series of hydrothermal experiments have been conducted in order to determine quartz solubility in the vapor-liquid region of the NaCl-H_2O system between 420 and 500 °C, 31.0–51.0 MPa. The experiments were performed in a newly designed fixed volume titanium reactor that proved extremely durable when exposed to extreme physical conditions for extended periods. The good agreement between experimental quartz solubility and the density equations of Von Damm et al. (1991) and Fournier (1983) significantly expands the pressure range over which the density equations are valid. Application of the Si-Cl geothermobarometer to the Piccard hydrothermal field, Mid-Cayman Rise indicates fluids encounter subsurface conditions of 540 ± 15 °C, 62.5 ± 3.0 MPa. These are the hottest and deepest conditions encountered by any MOR hydrothermal vent fluid. Using the Si-Cl results and the height of the Piccard plume, the overall heat flux is estimated to be 100 ± 37 MW, with an associated fluid flux of 1.2 ± 0.4 × 10^9 kg/year. Incorporating the heat lost during conductive cooling into the overall hydrothermal heat budget represents a novel approach and provides a more accurate measure of heat, hydrothermal fluid, and geochemical fluxes as compared to calculations based on measured conditions on the seafloor.

Acknowledgments
We thank Elizabeth Lundstrom for chemical analysis of the experimental samples and gratefully acknowledge funding provided by the National Science Foundation, grant OCE 1736679 (W. E. S.). We also thank L. Diamond, an anonymous reviewer, and Associate Editor Marie Edmonds for constructive comments. Data used are listed in the tables or in the supporting information.

References

Akinfiev, N. N., & Diamond, L. W. (2009). A simple predictive model of quartz solubility in water–salt–CO_2 systems at temperatures up to 1000 °C and pressures up to 1000 MPa. *Geochimica et Cosmochimica Acta*, *73*(6), 1597–1608. https://doi.org/10.1016/j.gca.2008.12.011

Alt, J. C., Laverne, C., Coggon, R. M., Teagle, D. A. H., Banerjee, N. R., Morgan, S., et al. (2010). Subsurface structure of a submarine hydrothermal system in ocean crust formed at the East Pacific Rise, ODP/IODP Site 1256. *Geochemistry, Geophysics, Geosystems*, *11*, Q10010. https://doi.org/10.1029/2010GC003144

Baker, E. T. (2007). Hydrothermal cooling of midocean ridge axes: Do measured and modeled heat fluxes agree? *Earth and Planetary Science Letters*, *263*(1-2), 140–150. https://doi.org/10.1016/j.epsl.2007.09.010

Berndt, M. E., Seyfried, W. E., & Janecky, D. R. (1989). Plagioclase and epidote buffering of cation ratios in mid-ocean ridge hydrothermal fluids: Experimental results in and near the supercritical region. *Geochimica et Cosmochimica Acta*, *53*(9), 2283–2300. https://doi.org/10.1016/0016-7037(89)90351-7

Bischoff, J. L. (1991). Densities of liquids and vapors in boiling NaCl-H_2O solutions; a PVTx summary from 300 degrees to 500 degrees C. *American Journal of Science*, *291*(4), 309–338. https://doi.org/10.2475/ajs.291.4.309

Bischoff, J. L., & Pitzer, K. S. (1989). Liquid-vapor relations for the system NaCl-H_2O; summary of the P-T-x surface from 300 degrees to 500 degrees C. *American Journal of Science*, *289*(3), 217–248. https://doi.org/10.2475/ajs.289.3.217

Bischoff, J. L., Rosenbauer, R. J., & Pitzer, K. S. (1986). The system NaCl-H2O: Relations of vapor-liquid near the critical temperature of water and of vapor-liquid-halite from 300° to 500°C. *Geochimica et Cosmochimica Acta*, *50*(7), 1437–1444. https://doi.org/10.1016/0016-7037(86)90317-0

Bischoff, J. L., & Seyfried, W. E. (1978). Hydrothermal chemistry of seawater from 25 degrees to 350 degrees C. *American Journal of Science*, *278*(6), 838–860. https://doi.org/10.2475/ajs.278.6.838

Bowers, T. S., Campbell, A. C., Measures, C. I., Spivack, A. J., Khadem, M., & Edmond, J. M. (1988). Chemical controls on the composition of vent fluids at 13°–11°N and 21°N, East Pacific Rise. *Journal of Geophysical Research*, *93*(B5), 4522–4536. https://doi.org/10.1029/JB093iB05p04522

Canales, P. J., Detrick Robert, S., Carbotte Suzanne, M., Kent Graham, M., Diebold John, B., Alistair, H., et al. (2005). Upper crustal structure and axial topography at intermediate spreading ridges: Seismic constraints from the southern Juan de Fuca Ridge. *Journal of Geophysical Research*, *110*, B12104. https://doi.org/10.1029/2005JB003630

Connelly, D. P., Copley, J. T., Murton, B. J., Stansfield, K., Tyler, P. A., German, C. R., et al. (2012). Hydrothermal vent fields and chemosynthetic biota on the world's deepest seafloor spreading centre. *Nature Communications*, *3*(1), 620. https://doi.org/10.1038/ncomms1636

de Martin, B. J., Sohn, R. A., Canales, J. P., & Humphris, S. E. (2007). Kinematics and geometry of active detachment faulting beneath the Trans-Atlantic Geotraverse (TAG) hydrothermal field on the Mid-Atlantic Ridge. *Geology*, *35*(8), 711–714. https://doi.org/10.1130/G23718A.1

Detrick, R. S., Buhl, P., Vera, E., Mutter, J., Orcutt, J., Madsen, J., & et al. (1987). Multi-channel seismic imaging of a crustal magma chamber along the East Pacific Rise. *Nature*, *326*(6108), 35–41. https://doi.org/10.1038/326035a0

Dolejs, D. (2013). Thermodynamics of aqueous species at high temperatures and pressures: Equations of state and transport theory. *Reviews in Mineralogy and Geochemistry*, *76*(1), 35–79. https://doi.org/10.2138/rmg.2013.76.3

Driesner, T. (2007). The system H_2O–NaCl. Part II: Correlations for molar volume, enthalpy, and isobaric heat capacity from 0 to 1000 °C, 1 to 5000 bar, and 0 to 1 XNaCl. *Geochimica et Cosmochimica Acta*, *71*(20), 4902–4919. https://doi.org/10.1016/j.gca.2007.05.026

Driesner, T., & Heinrich, C. A. (2007). The system H_2O–NaCl. Part I: Correlation formulae for phase relations in temperature–pressure–composition space from 0 to 1000 °C, 0 to 5000 bar, and 0 to 1 XNaCl. *Geochimica et Cosmochimica Acta*, *71*(20), 4880–4901. https://doi.org/10.1016/j.gca.2006.01.033

Elderfield, H., & Schultz, A. (1996). Mid-Ocean ridge hydrothermal fluxes and the chemical composition of the ocean. *Annual Review of Earth and Planetary Sciences*, *24*(1), 191–224. https://doi.org/10.1146/annurev.earth.24.1.191

Elthon, D., Ross, D. K., & Meen, J. K. (1995). Compositional variations of basaltic glasses from the Mid-Cayman Rise spreading center. *Journal of Geophysical Research*, *100*(B7), 12,497–12,512. https://doi.org/10.1029/94JB02777

Estapa, M. L., Breier, J. A., & German, C. R. (2015). Particle dynamics in the rising plume at Piccard hydrothermal field, Mid-Cayman Rise. *Geochemistry, Geophysics, Geosystems*, *16*, 2762–2774. https://doi.org/10.1002/2015GC005831

Fischer, H., List, J., Koh, R., Imberger, J., & Brooks, N. (1979). *Mixing in inland and coastal waters*. New York, NY: Academic Press.

Fontaine, F. J., Wilcock, W. S. D., Foustoukos, D. E., & Butterfield, D. A. (2009). A Si-Cl geothermobarometer for the reaction zone of high-temperature, basaltic-hosted mid-ocean ridge hydrothermal systems: Si/Cl-inferred P-T in MOR hydrothermal systems. *Geochemistry, Geophysics, Geosystems*, *10*, Q05009. https://doi.org/10.1029/2009GC002407

Fournier, R. O. (1983). A method of calculating quartz solubilities in aqueous sodium chloride solutions. *Geochimica et Cosmochimica Acta*, *47*(3), 579–586. https://doi.org/10.1016/0016-7037(83)90279-X

Fournier, R. O., & Potter, R. W. (1982). An equation correlating the solubility of quartz in water from 25° to 900°C at pressures up to 10,000 bars. *Geochimica et Cosmochimica Acta*, *46*(10), 1969–1973. https://doi.org/10.1016/0016-7037(82)90135-1

Foustoukos, D. I., Pester, N. J., Ding, K., & Seyfried, W. E. (2009). Dissolved carbon species in associated diffuse and focused flow hydrothermal vents at the Main Endeavour Field, Juan de Fuca Ridge: Phase equilibria and kinetic constraints. *Geochemistry, Geophysics, Geosystems*, *10*, Q10003. https://doi.org/10.1029/2009GC002472

Foustoukos, D. I., & Seyfried, W. E. (2007). Quartz solubility in the two-phase and critical region of the NaCl–KCl–H_2O system: Implications for submarine hydrothermal vent systems at 9°50′N East Pacific rise. *Geochimica et Cosmochimica Acta*, *71*(1), 186–201. https://doi.org/10.1016/j.gca.2006.08.038

Friðleifsson, G. Ó., Elders, W. A., Zierenberg, R. A., Stefánsson, A., Fowler, A. P. G., Weisenberger, T. B., et al. (2017). The Iceland Deep Drilling Project 4.5 km deep well, IDDP-2, in the seawater-recharged Reykjanes geothermal field in SW Iceland has successfully reached its supercritical target. *Scientific Drilling*, *23*, 1–12. https://doi.org/10.5194/sd-23-1-2017

Geiger, S., Driesner, T., Heinrich, C. A., & Matthäi, S. K. (2005). On the dynamics of NaCl-H_2O fluid convection in the Earth's crust. *Journal of Geophysical Research*, *110*, B07101. https://doi.org/10.1029/2004JB003362

German, C. R., Bowen, A., Coleman, M. L., Honig, D. L., Huber, J. A., Jakuba, M. V., et al. (2010). Diverse styles of submarine venting on the ultraslow spreading Mid-Cayman Rise. *Proceedings of the National Academy of Sciences of the United States of America*, *107*(32), 14,020–14,025. https://doi.org/10.1073/pnas.1009205107

German, C. R., & Seyfried, W. E. (2014). 8.7—Hydrothermal processes. In H. D. Holland & K. K. Turekian (Eds.), *Treatise on geochemistry* (2nd ed., pp. 191–233). Oxford: Elsevier.

German, C. R., Thurnherr, A. M., Knoery, J., Charlou, J.-L., Jean-Baptiste, P., & Edmonds, H. N. (2010). Heat, volume and chemical fluxes from submarine venting: A synthesis of results from the Rainbow hydrothermal field, 36°N MAR. *Deep Sea Research Part I: Oceanographic Research Papers*, *57*(4), 518–527. https://doi.org/10.1016/j.dsr.2009.12.011

Germanovich, L. N., Hurt, R. S., Smith, J. E., Genc, G., & Lowell, R. P. (2015). Measuring fluid flow and heat output in seafloor hydrothermal environments. *Journal of Geophysical Research: Solid Earth*, *120*, 8031–8055. https://doi.org/10.1002/2015JB012245

Hansen, H. P., & Koroleff, F. (1999). Determination of nutrients. In K. Grasshoff, K. Kremling, & M. Ehrhardt (Eds.), *Methods of seawater analysis* (pp. 159–228). Wiley-VCH Verlag GmbH.

Hayman, N. W., Grindlay, N. R., Perfit, M. R., Mann, P., Leroy, S., & de Lépinay, B. M. (2011). Oceanic core complex development at the ultraslow spreading Mid-Cayman Spreading Center. *Geochemistry, Geophysics, Geosystems*, *12*, Q0AG02. https://doi.org/10.1029/2010GC003240

Helgeson, H. C., & Kirkham, D. H. (1974). Theoretical prediction of the thermodynamic behavior of aqueous electrolytes at high pressures and temperatures; I, Summary of the thermodynamic/electrostatic properties of the solvent. *American Journal of Science*, *274*(10), 1089–1198. https://doi.org/10.2475/ajs.274.10.1089

Ito, E., & Anderson, A. T. (1983). Submarine metamorphism of gabbros from the Mid-Cayman Rise: Petrographic and mineralogic constraints on hydrothermal processes at slow-spreading ridges. *Contributions to Mineralogy and Petrology*, *82*(4), 371–388. https://doi.org/10.1007/BF00399714

Jean-Baptiste, P., Fourré, E., Charlou, J.-L., German, C. R., & Radford-Knoery, J. (2004). Helium isotopes at the Rainbow hydrothermal site (Mid-Atlantic Ridge, 36°14′N). *Earth and Planetary Science Letters*, *221*(1-4), 325–335. https://doi.org/10.1016/S0012-821X(04)00094-9

Junglas, P. (2009). WATER95—A MATLAB implementation of the IAPWS-95 standard for use in thermodynamics lectures. *International Journal of Engineering Education*, *1*, 3–10.

Kelley, D. S., Robinson, P. T., & Malpas, J. G. (1992). Processes of brine generation and circulation in the oceanic crust: Fluid inclusion evidence from the Troodos Ophiolite, Cyprus. *Journal of Geophysical Research*, *97*(B6), 9307–9322. https://doi.org/10.1029/92JB00520

Kent, G. M., Harding, A. J., & Orcutt, J. A. (1993). Distribution of magma beneath the East Pacific rise between the Clipperton Transform and the 9°17′N Deval from forward modeling of common depth point data. *Journal of Geophysical Research*, *98*(B8), 13,945–13,969. https://doi.org/10.1029/93JB00705

Kinsey, J. C., & German, C. R. (2013). Sustained volcanically-hosted venting at ultraslow ridges: Piccard hydrothermal field, Mid-Cayman Rise. *Earth and Planetary Science Letters*, *380*, 162–168. https://doi.org/10.1016/j.epsl.2013.08.001

Liebscher, A., & Heinrich, C. (2007). Fluid-fluid interactions in the earth's lithosphere. In A. Liebscher & C. Heinrich (Eds.), *Fluid-fluid interactions* (pp. 1–12). Chantilly, VA: Reviews in Mineralogy and Geochemistry. Mineralogical Society of America, Geochemical Society.

Little, S. A., Stolzenbach, K. D., & Von Herzen, R. P. (1987). Measurements of plume flow from a hydrothermal vent field. *Journal ofGeophysical Research*, *92*(B3), 2587–2596. https://doi.org/10.1029/JB092iB03p02587

Lowell, R. P., Rona, P. A., & Von Herzen, R. P. (1995). Seafloor hydrothermal systems. *Journal of Geophysical Research*, *100*(B1), 327–352. https://doi.org/10.1029/94JB02222

Manning, C. E. (1994). The solubility of quartz in H_2O in the lower crust and upper mantle. *Geochimica et Cosmochimica Acta*, *58*(22), 4831–4839. https://doi.org/10.1016/0016-7037(94)90214-3

McDermott J. (2015) Geochemistry of deep-sea hydrothermal vents fluids from the Mid-Cayman Rise, Caribbean Sea, (PhD thesis). Woods Hole Oceanographic Institute/MIT. https://doi.org/10.1575/1912/7128.

McDermott, J. M., Sylva, S. P., Ono, S., German, C. R., & Seewald, J. S. (2018). Geochemistry of fluids from Earth's deepest ridge-crest hot-springs: Piccard hydrothermal field, Mid-Cayman Rise. *Geochimica et Cosmochimica Acta*, *228*, 95–118. https://doi.org/10.1016/j.gca.2018.01.021

Mottl, M. J. (2003). Partitioning of energy and mass fluxes between mid-ocean ridge axes and flanks at high and low temperature. In *Energy and mass transfer in marine hydrothermal systems, Dahlem Workshop Report* (pp. 271–284). Berlin: Dahlem University Press.

Nielsen, S. G., Rehkämper, M., Teagle, D. A. H., Butterfield, D. A., Alt, J. C., & Halliday, A. N. (2006). Hydrothermal fluid fluxes calculated from the isotopic mass balance of thallium in the ocean crust. *Earth and Planetary Science Letters*, *251*(1-2), 120–133. https://doi.org/10.1016/j.epsl.2006.09.002

Olander, A., & Liander, H. (1950). The phase diagram of sodium chloride and steam above the critical point. *Acta Chemica Scandinavica*, *4*, 1437–1445. https://doi.org/10.3891/acta.chem.scand.04-1437

Palmer D. A. and Simonson J. M. (1996) Assessment of the ray diagram. Electric Power Research Institute, TR-106017.

Pester, N. J., Ding, K., & Seyfried, W. E. Jr. (2015). Vapor–liquid partitioning of alkaline earth and transition metals in NaCl-dominated hydrothermal fluids: An experimental study from 360 to 465 °C, near-critical to halite saturated conditions. *Geochimica et Cosmochimica Acta*, *168*, 111–132. https://doi.org/10.1016/j.gca.2015.07.028

Pester, N. J., Rough, M., Ding, K., & Seyfried, W. E. (2011). A new Fe/Mn geothermometer for hydrothermal systems: Implications for high-salinity fluids at 13°N on the East Pacific rise. *Geochimica et Cosmochimica Acta*, *75*(24), 7881–7892. https://doi.org/10.1016/j.gca.2011.08.043

Pokrovski, G. S., Roux, J., & Harrichoury, J.-C. (2005). Fluid density control on vapor-liquid partitioning of metals in hydrothermal systems. *Geology*, *33*(8), 657–660. https://doi.org/10.1130/G21475.1

Richardson, C. J., Cann, J. R., Richards, H. G., & Cowan, J. G. (1987). Metal-depleted root zones of the Troodos ore-forming hydrothermal systems, Cyprus. *Earth and Planetary Science Letters*, *84*(2-3), 243–253. https://doi.org/10.1016/0012-821X(87)90089-6

Rosenbauer, R. J., & Bischoff, J. L. (1987). Pressure-composition relations for coexisting gases and liquids and the critical points in the system NaCl-H2O at 450, 475, and 500°C. *Geochimica et Cosmochimica Acta*, *51*(9), 2349–2354. https://doi.org/10.1016/0016-7037(87)90289-4

Rudnicki, M. D., & German, C. R. (2002). Temporal variability of the hydrothermal plume above the Kairei vent field, 25°S, Central Indian Ridge. *Geochemistry, Geophysics, Geosystems*, *3*(2), 1010. https://doi.org/10.1029/2001GC000240

Schultz, A., Delaney, J. R., & McDuff, R. E. (1992). On the partitioning of heat flux between diffuse and point source seafloor venting. *Journal of Geophysical Research*, *97*(B9), 12,299–12,314. https://doi.org/10.1029/92JB00889

Seyfried, W. E. Jr., Janecky, D. R., & Berndt, M. E. (1987). Rocking autoclaves for hydrothermal experiments II: The flexible reaction-cell system. In G. C. Ulmer & H. L. Barnes (Eds.), *Hydrothermal experimental techniques* (pp. 216–240). Wiley Interscience.

Shmulovich, K. I., Sorokin, V. I., & Zaraisky, G. P. (1995). Hydrothermal experimental techniques used at the Institute of Experimental Mineralogy, Russian Academy of Sciences. In K. Shmulovich, B. W. Yardley, & G. G. Gonchar (Eds.), *Fluids in the Crust* (pp. 43–56). London: Chapman and Hall.

Sourirajan, S., & Kennedy, G. C. (1962). The system H_2O-NaCl at elevated temperatures and pressures. *American Journal of Science*, *260*(2), 115–141. https://doi.org/10.2475/ajs.260.2.115

Stroup, J. B., & Fox, P. J. (1981). Geologic investigations in the Cayman Trough: Evidence for thin oceanic crust along the Mid-Cayman Rise. *The Journal of Geology*, *89*(4), 395–420. https://doi.org/10.1086/628605

Styrikovich, M., Khaibullin, I. K., & Tskhvirashvili, D. (1955). Solubility of salts in high-pressure steam. *Doklady Akademii Nauk USSR*, *100*, 1123–1126.

Sverjensky, D. A., Harrison, B., & Azzolini, D. (2014). Water in the deep Earth: The dielectric constant and the solubilities of quartz and corundum to 60 kb and 1200 °C. *Geochimica et Cosmochimica Acta*, *129*, 125–145. https://doi.org/10.1016/j.gca.2013.12.019

ten Brink, U. S., Coleman, D. F., & Dillon, W. P. (2002). The nature of the crust under Cayman Trough from gravity. *Marine and Petroleum Geology*, *19*(8), 971–987. https://doi.org/10.1016/S0264-8172(02)00132-0

Veirs, S. R., McDuff, R. E., & Stahr, F. R. (2006). Magnitude and variance of near-bottom horizontal heat flux at the Main Endeavour hydrothermal vent field. *Geochemistry, Geophysics, Geosystems*, *7*, Q02004. https://doi.org/10.1029/2005GC000952

Von Damm, K. L. (1988). Systematics of and postulated controls on submarine hydrothermal solution chemistry. *Journal of Geophysical Research*, *93*(B5), 4551–4561. https://doi.org/10.1029/JB093iB05p04551

Von Damm, K. L. (1995). Controls on the chemistry and temporal variability of seafloor hydrothermal fluids. *Seafloor Hydrothermal Systems: Physical, Chemical, Biological, and Geological Interactions*, 222–247.

Von Damm, K. L. V., Bischoff, J. L., & Rosenbauer, R. J. (1991). Quartz solubility in hydrothermal seawater; an experimental study and equation describing quartz solubility for up to 0.5 M NaCl solutions. *American Journal Science*, *291*(10), 977–1007. https://doi.org/10.2475/ajs.291.10.977

Wagner, W., & Pruss, A. (2002). The IAPWS formulation 1995 for the thermodynamic properties of ordinary water substance for general and scientific use. *Journal of Physical and Chemical Reference Data*, *31*(2), 387–535. https://doi.org/10.1063/1.1461829

Xie, Z., & Walther, J. V. (1993). Quartz solubilities in NaCl solutions with and without wollastonite at elevated temperatures and pressures. *Geochimica et Cosmochimica Acta*, *57*(9), 1947–1955. https://doi.org/10.1016/0016-7037(93)90086-C